Chapter 4

RAMAN SPECTROSCOPY OF CARBON NANOTUBES

M. S. Dresselhaus, G. Dresselhaus, R. Saito and A. Jorio

1. INTRODUCTION

Raman spectroscopy has been widely used by most carbon nanotube researchers to characterize their samples broadly, from their basic synthesis and purification processes all the way to their ultimate use in nanotube modifications and device applications. The broad interest from the carbon nanotube research community in Raman spectroscopy comes from the capability of this technique to easily and nondestructively characterize carbon nanotube samples with respect to diameter and chirality distribution, population of specific (n, m) species in a sample, sample purity, doping, functionalization, as well as temperature, pressure and strain effects. To achieve such a characterization capability, research has focused on understanding the basic physical properties of carbon nanotubes, primarily by advancing our knowledge of their electronic, vibrational and geometric structure, and of the interrelation between these properties.

AU :1

The unique optical and spectroscopic properties observed in single wall carbon nanotubes (SWNTs) are largely due to the one-dimensional (1D) confinement of electronic and phonon states and due to the so-called resonance Raman process. Because of this 1D confinement, the resonance effect is both strongly enhanced relative to graphite and highly selective of the SWNT geometric structure, namely its diameter and chirality. Thus Raman spectroscopy has become not only a spectroscopic tool, but also has become a structural characterization tool for SWNTs. In this article we show how carbon nanotubes are a unique system for the study of the rich Raman spectra of 1D systems, and at the same time Raman spectroscopy has provided an exceedingly powerful tool for the detailed characterization of SWNTs.

Raman scattering refers to the inelastic scattering of light in molecules and solids. By exciting (or absorbing) an elementary excitation of the material (usually a phonon, the quantum of lattice vibration), the scattered light loses (or gains) the

1   characteristic energy of the excitation ΔE relative to the energy of the incident light
     (E_{laser}). Raman spectra refer to the spectral intensity of the scattered light as a
3   function of energy shift ΔE, usually measured in units of $cm^{-1} = (1/8065)\,eV$. These
     spectra are observed by using a laser, a monochromator, a spectrometer, and a
5   detector. A monochromator (or some optical filter) is needed for removing the
     strong elastically scattered Rayleigh light, appearing near $\Delta E = 0$.
7   Fig. 1a gives a general view of the Raman spectra from a typical SWNT bundle
     sample taken with different laser excitation lines (E_{laser}) and Fig. 1b shows spectra
9   taken at the individual nanotube level. There are two dominant Raman signatures
     that distinguish a SWNT from other forms of carbon. The first relates to the low
11   frequency feature, usually in the range $100\text{–}300\,cm^{-1}$, arising from scattering by
     the radial breathing modes (RBM) which correspond to symmetric in-phase

13
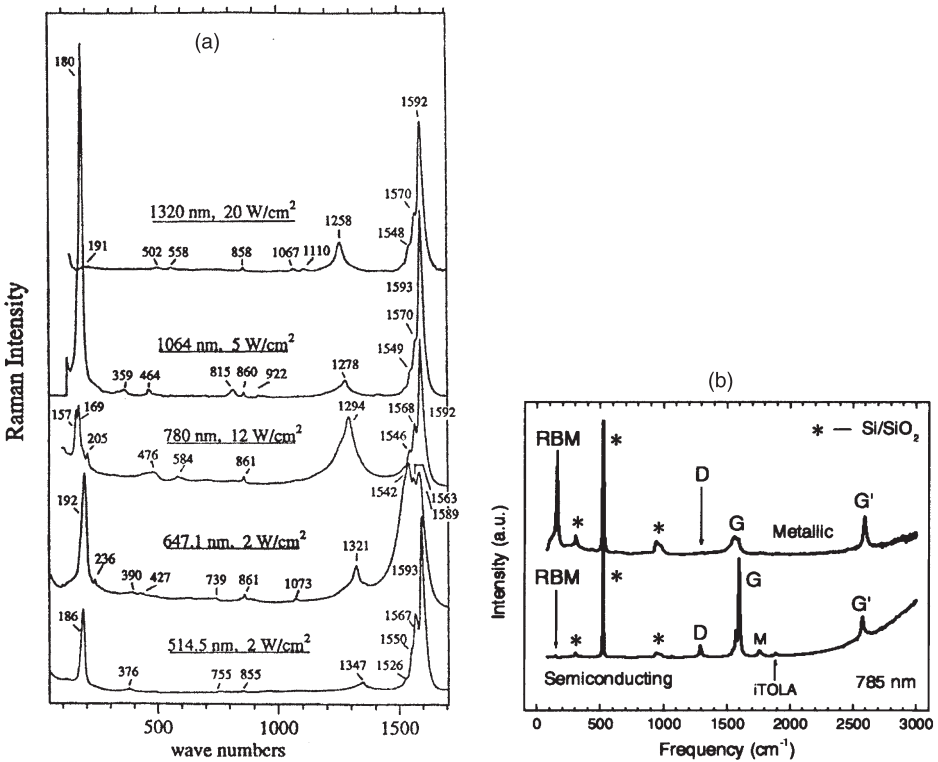
15

17

19

21

23

25

27

29

31

33

35

37

39

Fig. 1.   (a) Room temperature Raman spectra from SWNT bundles grown by the laser
vaporization method, excited at five different laser energies (wavelengths) [1], as indicated
along with the power density and the vibrational frequencies (in cm^{-1}). (b) Raman spectra
from a metallic (top) and a semiconducting (bottom) SWNT at the single nanotube level. The
dominant spectral features are indicated and are discussed in this chapter. The Raman
features denoted by "*" come from the Si/SiO$_2$ substrate [2].

1 displacements of all the carbon atoms in the SWNT in the radial direction. The second signature relates to the multiple higher frequency features (around 1500–
3 1600 cm^{-1}) associated with the tangential (*G*-band) vibrational modes. Neither the RBM feature nor the *multiple G*-band features are observed in any other sp^2 bonded
5 carbon material, which shows a characteristic *single G*-band (Lorentzian shape) Raman peak at 1582 cm^{-1} (discussed in Section 3.3.2). These two first-order Raman
7 features (the RBM and the multi *G*-band) are, therefore, the spectral signatures of SWNTs and have been used to characterize nanotube samples from their earliest
9 stage of identification [3,4].

From an historical perspective, the use of Raman spectroscopy to characterize
11 carbon materials [5] generally motivated researchers to apply this technique also to SWNTs shortly after the early synthesis of SWNTs in 1993 [6,7]. Even though only
13 ∼1% of the carbonaceous material in the sample was estimated to be due to SWNTs [3], a unique Raman spectrum was observed, different from any other
15 previously observed spectrum for a carbon material, thereby motivating further development of this noninvasive characterization technique for SWNTs.
17 The power of this technique to study and characterize carbon nanotube samples and nanotube properties became evident in 1997, when the process was shown to be
19 highly selective not only of SWNTs embedded in a sample containing other carbonaceous species, but of specific (*n*, *m*) SWNTs due to the resonance Raman
21 effect [1]. Since the resonance Raman intensity depends on the density of electronic states (DOS) available for the optical transitions, and this resonance property is
23 especially important for 1D systems where quantum confinement effects give rise to singularities in the DOS. Fig. 1a shows that when E_{laser} is varied, the Raman spectra
25 change dramatically, because different laser excitation energies are in resonance with different SWNTs depending on their tube diameters d_t and chiral angles θ. Resonance
27 Raman spectroscopy (RRS) has thus become a very powerful tool to study the vibrational and electronic properties of SWNTs. The next breakthrough came in 2001
29 with the observation of the Raman spectrum from one isolated SWNT sitting on a SiO$_2$ substrate [2] (see Fig. 1b), greatly advancing our understanding of Raman
31 spectroscopy in 1D materials generally, since SWNT properties could now be measured in great detail at the single nanotube level from an object only ∼1 nm in
33 diameter with a well-defined geometrical structure [1].

To understand the very special Raman spectra of carbon nanotubes, the physics
35 we learn from SWNTs, and how to use this technique to characterize SWNT samples [8,9], some basic concepts of the Raman scattering effect are introduced in
37 Section 2. This is followed by a discussion of how resonance Raman scattering has been used to study and characterize (Section 3) carbon nanotubes.
39

41 # 2. BASIC CONCEPTS OF RESONANCE
RAMAN SCATTERING
43

In this section the constituent optical processes in Raman scattering are introduced,
45 and resonant processes are distinguished from nonresonant processes. Resonance

1 with both the incident and scattered photon are considered, along with first-order and higher-order scattering processes for phonon emission (Stokes process) and
3 phonon absorption (anti-Stokes process).

   A Raman scattering event consists of three basic optical processes: (1) photon
5 absorption to excite an exciton (an electron bound to the hole that is simultaneously created by the photon), (2) phonon emission from an exciton, and (3) finally photon
7 emission by the exciton. We measure the emitted photons as a Raman spectrum in which the Raman scattering intensity is plotted vs. energy shift ΔE (see Section 1 and
9 Fig. 1). In light scattering, the photon absorption process generally occurs even though the energy separation between the ground and excited states is not equal to
11 the photon energy, in which case we call the transition a *virtual* or *nonresonant* transition.

13   It is easy to understand a nonresonant transition for a mechanical system, consisting of a spring and a ball. Even though we force this system to vibrate with a
15 frequency which is not a natural eigen-frequency of the system, the vibration will still have some vibrational amplitude. When the vibrational frequency is close to an
17 eigen-frequency of the system, the vibrational amplitude becomes singularly large. This enhancement in intensity is identified with a resonance phenomenon.

19   A similar effect occurs for the Raman process, and it is called RRS. Here the scattered amplitude becomes very large when E_{laser} is close to the transition energy
21 for light absorption or emission (E_{ii}). There are two possible conditions for resonance, and these are called, the incident and scattered resonance conditions in
23 which either the incident or scattered photons, respectively, have the same energy as the energy level separation of the system. For photon absorption, where the incident
25 light resonance condition is:

27 $$E_{\text{laser}} = E_{ii} \qquad \text{(incident light resonance)} \qquad (1)$$

29 all Raman features will be resonantly enhanced. However, for the scattered light resonance condition for the creation of a phonon with frequency ω_i,
31

33 $$E_{\text{laser}} = E_{ii} + \hbar\omega_i \qquad \text{(Stokes scattered light resonance)} \qquad (2)$$

   the resonance condition depends on the phonon energy $\hbar\omega_i$. Inelastic scattering of
35 light is also possible by absorbing a phonon, which is called anti-Stokes Raman scattering. Anti-Stokes Raman spectra can be seen relative to $\Delta E = 0$ on the
37 opposite side of the spectrum for phonon emission (Stokes Raman spectra). In order to absorb a phonon, the phonon should be present in the Bose–Einstein distribution
39 at thermal equilibrium. Thus anti-Stokes Raman spectra will have a very low intensity for high energy phonons and at low temperatures. The resonance condition
41 for the anti-Stokes Raman spectra for the incident light resonance condition is the same as that of the Stokes spectra. As for the scattered light resonance, the condition
43 is given by

45 $$E_{\text{laser}} = E_{ii} - \hbar\omega_i \qquad \text{(anti-Stokes scattered light resonance)} \qquad (3)$$

1 Thus by comparing the Stokes with the anti-Stokes spectra, we can know whether the resonance condition is for the incident resonance or scattered resonance.

3 The number of emitted phonons before relaxation of the lattice can be one, two, and so on, which we call, respectively, one-phonon, two-phonon, and multi-phonon

5 Raman processes. The order of a scattering event is defined as its number in the sequence of all the scattering events, including both phonon inelastic scattering and

7 elastic scattering by an imperfection (such as a defect or edge) of the crystal. The lowest order process is the first-order Raman scattering process which involves one-

9 phonon emission, such as the RBM, or the *G*-band feature shown in Fig. 1 for SWNTs. A scattering event with only elastic scattering, i.e., change of photon

11 direction but no frequency shift, corresponds to Rayleigh scattering.

Finally, incident and scattered light polarization is an important issue for Raman

13 scattering, because optical absorption and emission usually exhibit a polarization dependence. The so-called selection rules, which depend on light polarization, tell us

15 whether or not a given set of electronic levels that can be coupled by light.

17

3. RESONANCE RAMAN SPECTROSCOPY OF
19 CARBON NANOTUBES

21 In this section we focus on the various features appearing in the resonance Raman spectra of SWNTs. The spectra observed from SWNT bundle samples and at the

23 single nanotube level are discussed, focusing on the complementary information provided by ensembles of SWNTs and by a single nanotube.

25

27 *3.1. 1D van Hove Singularities and the Kataura Plot*

29 In the case of a SWNT, the energy separation which is relevant to RRS corresponds to the transition energies which appear as singularities [called van Hove singularities

31 (vHSs)] in the electronic density of states (DOS). These singularities in the DOS (see Fig. 2) come from the energy maxima or minima of 1D energy subbands of an

33 individual SWNT. The electronic structure of an (n, m) SWNT has many 1D energy subbands, and therefore many vHSs. However, despite the large number of vHSs,

35 only a small number of electronic levels can be connected by light due to the symmetry selection rules. Electrons (and phonons) in carbon nanotubes are

37 characterized by their 1D wave vectors (k for electrons and q for phonons) and by their symmetries, that relate to nothing else than the number of nodes for their

39 wave functions around the circumferential direction. The totally symmetric A states for electrons (and phonons) have no nodes, while the various harmonics usually

41 exhibit double degenerate symmetries E_μ, so that for levels labeled by $\mu = 1, 2, 3, \ldots$ the eigenvectors have 2, 4, 6, ... nodes [10,11]. It is known that light can be strongly

43 absorbed when the polarization of the electric field is parallel to the nanotube axis. In this case, valence and conduction electrons having the same symmetry ($E_\mu^v \rightarrow E_\mu^c$)

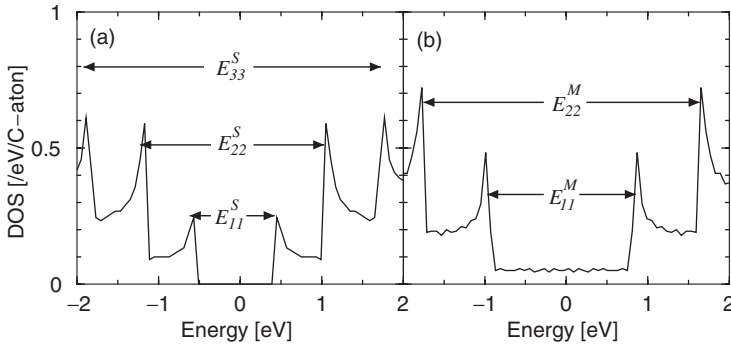45 are coupled by light. On the other hand, when the polarization vector is

Fig. 2. Electronic density of states for (a) a semiconducting SWNT and (b) a metallic SWNT. The Fermi energy (E_F) is located at $E = 0$. An optical transition is possible between vHS peaks in the valence and conduction bands. Energy separations between two vHS peaks are labeled from smallest to largest for semiconducting tubes by E_{11}^S, E_{22}^S, E_{33}^S, …, and for metallic tubes by E_{11}^M, E_{22}^M, … .

perpendicular to the nanotube axis, the absorption vanishes [12,13] in accordance with polarization selection rules which further tell us that the resonance energies for perpendicular polarization of the light couple $E_\mu^v \rightarrow E_{\mu\pm1}^c$.

Therefore, because of the selection rules for optical transitions [12,13], optical transitions occur between two peaks which are approximately symmetrically placed with respect to the Fermi energy E_F, as shown in Fig. 2. These transitions are labeled E_{11}, E_{22}, E_{33} and so on, according to how close in energy they are to E_F. Like a fingerprint, each carbon nanotube labeled by (n, m) has different E_{ii} values. We further note in Fig. 2, that the DOS at E_F for metallic tubes is nonzero and constant between the highest valence band vHS and the lowest conduction band vHS. The actual transition energies E_{ii} are excitonic in nature because the excited electron is bound to the hole that is left behind in the excitation process, giving rise to what is called a bound electron–hole pair or an exciton. The actual E_{ii} are further perturbed by electron–electron repulsion effects and it is these perturbed excitonic transition energies E_{ii} that are observed experimentally and calculated theoretically. These electron–hole and electron–electron interactions are specially important in 1D systems, since the electrons and holes are highly confined in 1D space.

To analyze the resonance Raman spectra of SWNTs, it is useful to have a plot of these resonant transition energies E_{ii} as a function of tube diameter d_t for all (n, m) SWNTs, and we call such a plot a Kataura plot (see Fig. 3). This plot was first proposed in 1999 by H. Kataura [14], and subsequent optical and Raman spectroscopic measurements had a large influence on the detailed development of this plot. From the Kataura plot in Fig. 3, we see that the resonant transition energies E_{ii} are approximately inversely proportional to d_t, and each E_{ii} band has some width due to the chirality dependence of E_{ii} [15]. For a given d_t, the sequence of E_{ii} is in the order E_{11}^S, E_{22}^S, E_{11}^M, E_{33}^S, etc. starting from the lowest energy. One typical use of a Kataura plot would be to tell a researcher that for a sample with a diameter
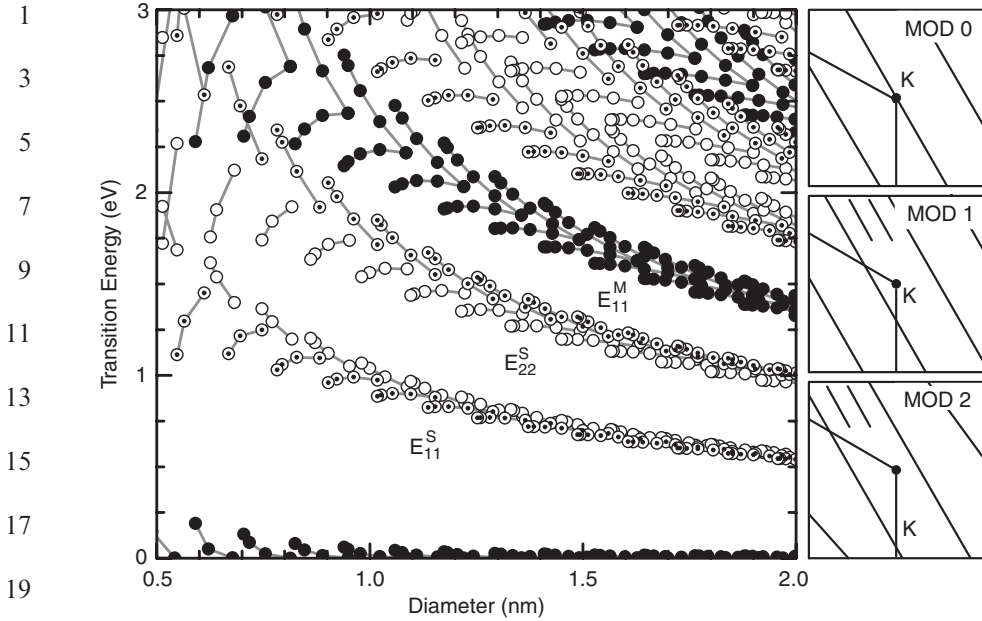
1
3
5
7
9
11
13
15
17
19

Fig. 3. Plot of the transition energies E_{ii} vs. d_t for all (n, m) values occurring for $0.5 < d_t < 2.0$ nm (Kataura plot) where S and M denote semiconducting, and metallic nanotubes, respectively. On the right, cutting lines are shown for M tubes (MOD0), and S tubes of two types, MOD1 and MOD2, for open and open-dot circles (see text).

distribution of, for example, $d_t = 1.4 \pm 0.1$ nm, a Raman signal from semiconducting (S) and metallic (M) SWNTs would be expected for $E_{laser} \sim 1.4$ eV (E_{22}^S) and 1.9 eV (E_{11}^M), respectively. Note that when we rotate the polarization of the light away from parallel to the SWNT axis, the resonance condition obtained for parallel polarization for a given E_{laser} (Fig. 3) will no longer apply [16].

3.2. Family Patterns

SWNTs are metallic when $(n-m)$ or equivalently when $(2n+m)$ is divisible by 3 (MOD0) and are semiconducting otherwise [10,17,18]. This fundamental result can be understood from the diagrams in Fig. 3 to the right of the Kataura plot, where the cutting lines, denoting allowed states for wave vectors in the circumferential direction of SWNTs, are shown to only pass through the K point in the 2D graphene Brillouin zone (BZ) for the case of MOD0, where the K point is the point in reciprocal space of 2D graphite, where the valence and conduction bands cross E_F to form a zero gap semiconductor [10]. For semiconducting SWNTs we distinguish the case where the remainder of the division of $(2n+m)/3$ is 1 or 2 by MOD1 (open circles in Fig. 3) and MOD2 (open-dot circles), respectively. We thus see that the energies E_{ii}^S follow a similar pattern (the so-called family behavior), according to the

1   $2n + m$ value of a SWNT (which labels its family) and whether the SWNT is MOD1
    or MOD2 [19,20]. Thus, a (6,5) SWNT would be designated by MOD2 and family
3   $2n + m = 17$. Each metallic SWNT has two vHSs in its DOS for each E_{ii}^{M}, except for
    armchair SWNTs. The occurrence of two vHSs for each E_{ii}^{M} is due to the so-called
5   trigonal warping effect of the electronic structure [15], and the energy separation
    between the two vHSs for a metallic tube generally increases as the chiral angle
7   decreases. Family patterns are observed in Fig. 3 for both S and M SWNTs. We note
    that each (n, m) nanotube in the long tube length limit has a unique set of E_{ii} values
9   and can in this sense be considered as a unique molecule. The connection between
    the resonance Raman spectra and the Kataura plot is further discussed below.

11

3.3. Raman Spectroscopy for Isolated Individual SWNTs
13

    Because of the strong resonance process in 1D systems, a large enhancement in the
15 Raman signal occurs, allowing the identification of the structure (diameter d_t and
    chiral angle θ) of individual SWNTs to be made, which in turn allows nanotube
17 properties to be determined as a function of d_t and θ.

19 *3.3.1. The RBM (n, m) Assignment and the Resonance Window*
    In this subsection we show how measurements at the single nanotube level allow a
21 determination to be made of the d_t and θ nanotube chirality, which is usually
    denoted in terms of the (n, m) indices of the SWNT [10]. In addition, single nanotube
23 spectroscopy allows measurements to be made of the resonant window of an
    individual SWNT, if a suitable "tunable" laser source is available.
25   In the process of measuring the Raman spectra from isolated SWNTs on a Si/SiO$_2$
    substrate using a fixed laser energy E_{laser}, the laser spot is focused on the substrate
27 surface (micro Raman spectroscopy) and is scanned over the sample until the Raman
    signal from an isolated SWNT is observed. The Raman intensity from SWNTs is
29 usually buried under the noise, except for a few (n, m) SWNTs, which have E_{ii} values
    within the resonance window of a given E_{laser}. Fig. 4b shows the Raman spectra from
31 three isolated SWNTs in resonance with an excitation laser $E_{laser} = 1.58$ eV, taken
    from different spots on the Si/SiO$_2$ substrate shown in Fig. 4a. From knowledge of
33 both the RBM frequency ω_{RBM} and $E_{ii} \sim E_{laser}$, the (n, m) geometrical structure can
    be defined, making use of the Kataura plot (Fig. 3) and a relation between ω_{RBM} and
35 d_t. The ω_{RBM} is known to depend linearly on the number of carbon atoms around the
    SWNT circumference, and therefore ω_{RBM} depends on $1/d_t$. In this work [2] the
37 relation used to relate ω_{RBM} to d_t for SWNTs in the diameter range $1.2 < d_t < 1.8$ nm
    was found to be $\omega_{RBM} = 2.48/d_t$. This assignment with $\omega_{RBM} = 248/d_t$ cm^{-1} works
39 well for $d_t > 1$ nm. However, for small diameter SWNTs ($d_t < 1$ nm), we need to
    consider in detail the curvature effect of the cylindrical surface of a SWNT on E_{ii} and
41 ω_{RBM}. The Kataura plot itself has been established by making resonance Raman (see
    Section 3.4) and photoluminescence (PL) [20] measurements on many tubes so that
43 the family patterns in Fig. 3 could be firmly established.
        By using a tunable laser, it is also possible to study the resonance window of *one*
45 isolated SWNT, giving the E_{ii} value with a precision better than 5 meV, as shown in
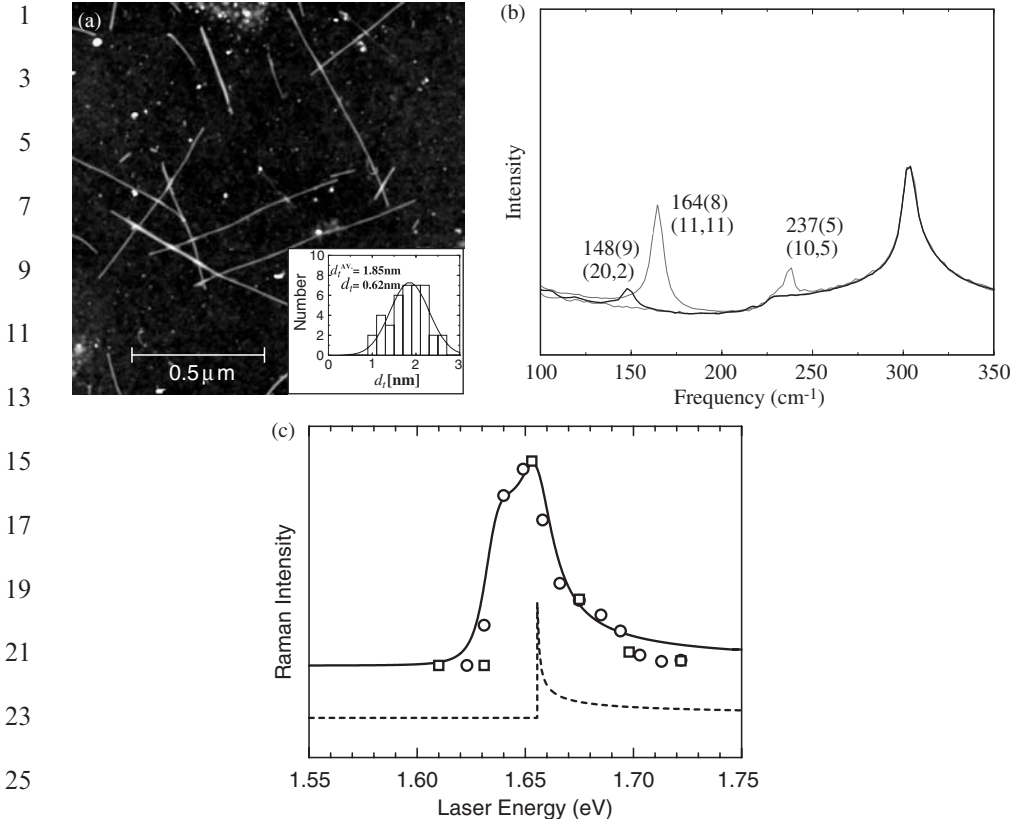
Fig. 4. (a) AFM image of SWNTs on a Si/SiO$_2$ substrate. The inset shows the SWNT diameter distribution of the sample. (b) Raman spectra from three different spots in (a). The RBM frequencies (widths) and the (n, m) assignment for each resonant SWNT are displayed [2]. The 303 cm^{-1} feature comes from the Si substrate and is used for calibration purposes. (c) Raman intensity vs. E_{laser} for the anti-Stokes RBM feature at the 173.6 cm^{-1} assigned to an isolated (18,0) SWNT on a Si/SiO$_2$ substrate [21]. The predicted resonant window (solid curve) and the vHS at 1.655 eV (dashed curve) are shown.

Fig. 4c [21]. Here the resonance window for the anti-Stokes process is shown to have a full width at half maximum intensity of only 8 meV and to be asymmetric in lineshape, reflecting the asymmetric lineshape of the van Hove singularity (dotted curve in Fig. 4c). To observe the asymmetry in the resonance window, its linewidth must be small. The appearance of spiky vHS peaks in the DOS is a general effect of quantum confined 1D energy bands, but this effect is enhanced in SWNTs because of their small d_t values.

3.3.2. The G-Band Raman Spectra at the Single Nanotube Level

The *G*-band refers to the in-plane optic phonon modes which are Raman-active in sp^2 graphitic materials. Since graphite is not an ionic material, the longitudinal (LO)

1 and transverse (TO) optic phonon modes are degenerate at the Γ point (zone center)
   of the BZ. Because of the curvature of the cylindrical surface of SWNTs, their
3 LO and TO phonon modes are split into higher and lower frequencies, G^+ and
   G^-, respectively. While the LO frequency ω_{G^+}, for vibrations along the tube axis, is
5 almost independent of d_t, the TO frequency ω_{G^-}, for vibrations in the circum-
   ferential direction, is downshifted because of its mode softening due to tube
7 curvature.
      RRS at the single nanotube level allows detailed measurements to be made of both
9 diameter and chirality effects and polarization effects, as summarized below. Such
   detailed studies are not possible for ensemble samples. The difference in the
11 lineshape for the G-band for graphite, which consists of a single simple Lorentzian
   line, and for SWNTs is dramatically shown in Fig. 5a. For both semiconducting and
13 metallic SWNTs, two dominant features are seen in Fig. 5a, corresponding to fully
   symmetric modes. For semiconducting SWNTs (Fig. 5b) the LO (or G^+) mode has a
15 stronger intensity, and the weaker mode is the TO (or G^-) mode discussed above,
   with an LO–TO splitting induced by tube curvature effects. This splitting increases
17 as $1/d_t^2$, as shown in Fig. 5c. Whereas the TO (or G^-) mode for semiconducting
   SWNTs has a Lorentzian lineshape, Fig. 5a shows that the lineshape for the G^-
19 mode for metallic tubes is very different and follows a Breit–Wigner–Fano lineshape,
   with a $1/d_t^2$ mode frequency dependence that is approximately twice as strong as for
21 the semiconducting SWNTs [22]. Fig. 5b shows that the LO–TO splitting can be
   used in addition to ω_{RBM} to characterize the nanotube diameter.
23   In the case of isolated SWNTs, the polarization of the light relative to the
   nanotube axis is important for studies of the Raman intensity. Absorption and/or
25 emission of light perpendicularly polarized with respect to the nanotube axis is
   responsible for the observation of Raman modes with E_1 and E_2 group theoretical
27 symmetry [10], while only phonons with A symmetry can be observed for parallel
   polarized light [11]. E_1 and E_2 phonons have indeed be seen in the G-band of both
29 isolated [23,24] and bundled [25] SWNTs, and their polarization dependence
   confirms the selection rules for this 1D system. However, the most general
31 polarization behavior for the optical properties of SWNTs is a strong angular
   dependence of the polarization, where the general Raman intensity drops for light
33 perpendicular to the nanotube axis [23,26], and this behavior is understood by the
   antenna effect of electromagnetic theory [27]. Such polarization effects could be
35 important for potential optical communications applications of SWNTs.

37

3.4. Setting up the Kataura Plot

39

   In setting up the Kataura plot (Fig. 3) we use information from the G-band spectra
41 to give the general placement of the E_{ii}^{M} and E_{ii}^{S} bands, and we use E_{ii} vs. ω_{RBM} in
   the RBM spectra to yield a specific point on the Kataura plot for each (n, m)
43 SWNT [28]. Measurements on many SWNTs allow ω_{RBM} to be related to d_t [28]
   and these relations are further supported by theoretical calculations [29]. PL
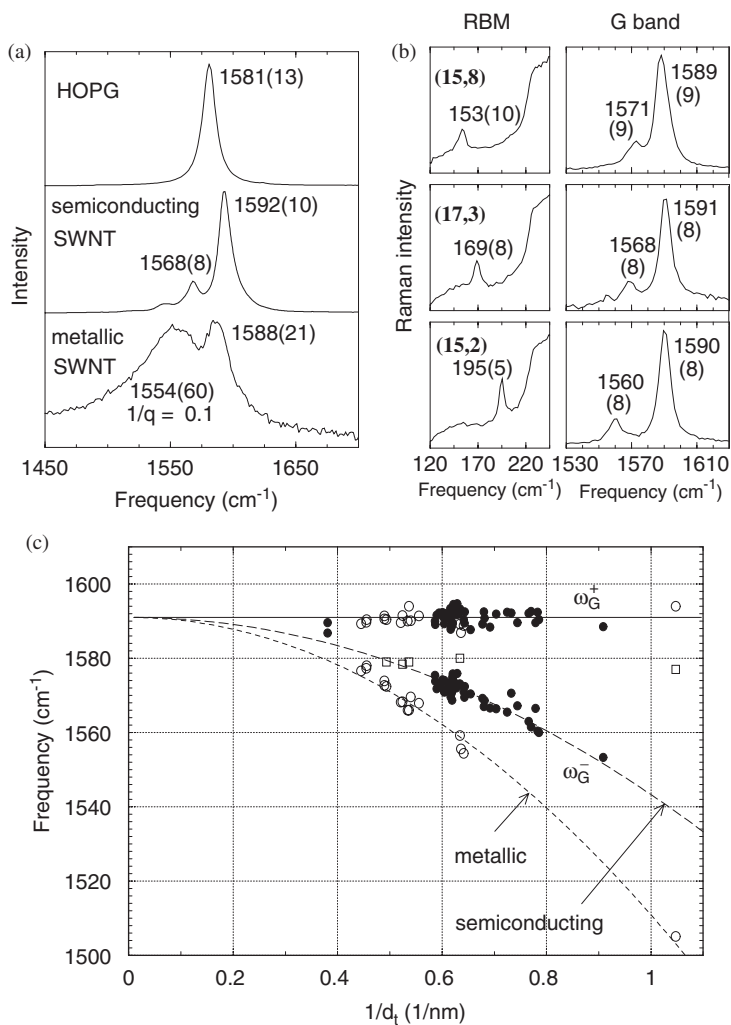45 measurements can only be made on semiconducting SWNTs [20] and for these

Fig. 5. (a) *G*-band Raman spectra for highly oriented pyrolytic graphite (HOPG), and for semiconducting and metallic SWNTs. (b) RBM and *G*-band spectra of isolated SWNTs for larger (top) to smaller (bottom) diameters. (c) *G*-band frequencies ω_{G^+} and ω_{G^-} for 62 isolated SWNT are plotted vs. $1/d_t$ [22].

SWNTs, the PL data yield points for the Kataura plot in agreement with the RRS data [20,28].

3.4.1. The G-Band and the Subband Positions

The determination of the relative subband positions utilizes the different lineshapes of M and S SWNTs, as shown in Figs. 5a and 6a. This difference in lineshape is best
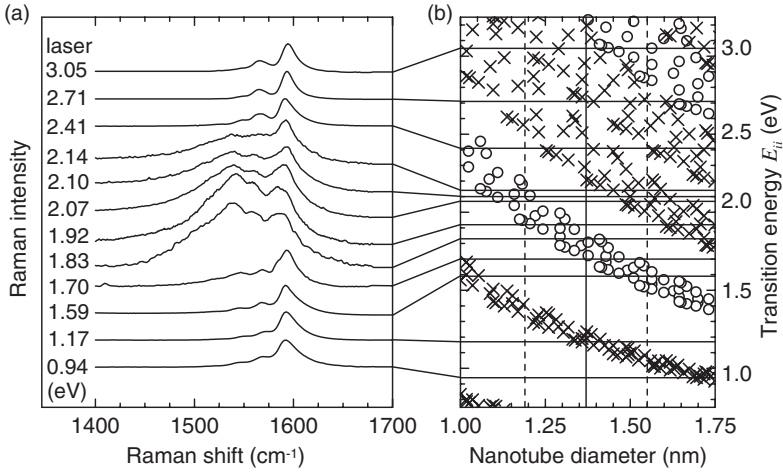
1

3

5

7

9

11

13

15

Fig. 6. (a) Raman spectra of the tangential *G*-band modes of SWNT bundles measured with several different laser lines, on a sample with $d_t = 1.37 \pm 0.18$ nm [32]. (b) Resonant transition energies E_{ii} vs. d_t. The vertical solid line is the average d_t and the vertical dashed lines denote the d_t distribution width. Crosses are for S SWNTs and open circles for M SWNTs.

21

observed in SWNT bundle samples since the coupling of the conduction electrons to
23 phonons through a plasmon excitation is enhanced by intertube interactions [30,31].
By measuring the Raman spectra of nanotube bundles through varying E_{laser}, as
25 shown in Fig. 6a, different E_{ii} for M and S tubes are probed at different E_{laser} values
[32], and this information is used to identify M and S SWNTs in Fig. 6b. Based on
27 the lineshape fits of the G^- feature for S and M SWNTs, the various traces in Fig. 6a
are identified in Fig. 6b with the resonant E_{ii} for semiconducting and metallic
29 SWNTs contained within the sample.

31

3.4.2. The RBM and the Kataura Plot
33 By using a Raman system with many laser lines, it is possible to obtain the E_{ii}
energies for many tubes, as shown in Fig. 7a where Raman intensity contours vs.
35 ω_{RBM} are shown. These data were obtained from resonance Raman spectra [28]
taken from a HiPco sample[1] with a diameter distribution $d_t = 1.0 \pm 0.2$ nm where the
37 individual tubes were wrapped with sodium dodecyl sulfate (SDS) [33]. A wrapping
agent is used to isolate one SWNT from another to enable PL measurements to be
39 made [33]. In this way Raman spectroscopy (RRS) and PL measurements could be
carried out on the same sample [28].
41   In order to avoid use of an empirical fitting procedure in implementing the
Kataura plot, we plot E_{ii} vs. ω_{RBM} (Fig. 7b) directly from the experimental values in
43 Fig. 7a for each (*n, m*) resonant SWNT [28]. Black circles and squares represent,
respectively, S and M SWNTs. Using 76 values of E_{laser} for $1.52 \le E_{laser} \le 2.71$ eV, a
45 2D plot is made from the RBM spectra obtained from Stokes resonance Raman
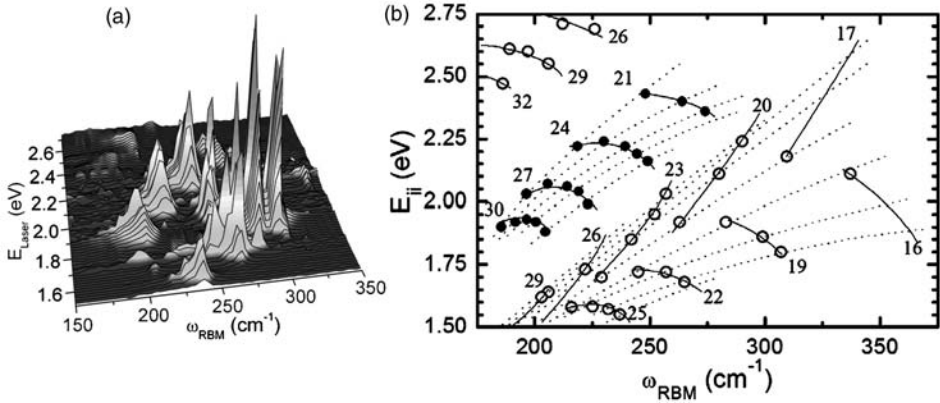
Fig. 7. (a) RBM resonance Raman measurements of HiPco SWNT nanotubes, wrapped in SDS and dispersed in an aqueous solution [33], taken with 76 different laser lines E_{laser} between 1.52 and 2.71 eV [28]. (b) The points denote 47 electronic transition energies E_{ii} vs. ω_{RBM} for 41 different (n, m) SWNTs in (a). Solid and open circles, respectively, denote metallic and semiconducting SWNTs. Each family is denoted by its $(2n + m) = $ constant value, allowing family patterns to be clearly seen.

measurements as a function of E_{laser}. Each RBM peak in Fig. 7a can be assigned to a (n, m) SWNT with the idea of family patterns (see Section 3.2). The family patterns of E_{ii} ($2n + m = $ constant) for semiconducting (E_{22}^S and E_{33}^S) and metallic (E_{11}^M) tubes are clearly seen in Fig. 7b, where we also show the values of $(2n + m)$. The different behaviors of the MOD1 and MOD2 semiconducting SWNTs (see Section 3.2) in the Kataura plot are clearly seen.

The (E_{ii}, ω_{RBM}) results (Fig. 7b) can be compared with a theoretical model that considers in detail the distortion of the C–C bonds due to the curvature of the graphene sheet when it is rolled up to form a SWNT [18,29]. The model also considers the effects of the excitonic binding of the excited electron–hole pair and the Coulomb repulsion of electrons. Both of these phenomena are referred to as many-body effects. The comparison between this theoretical model and the RRS experimental results leads to a clear (n, m) assignment for each tube.

From the (n, m) assignment for both metallic and semiconducting SWNTs through Fig. 7b, a simple relation $\omega_{RBM} = 218/d_t + 16 \, cm^{-1}$ is obtained to correlate ω_{RBM} with d_t for the small diameter tubes (d_t from 0.7 to 1.2 nm) for SWNTs wrapped with SDS in aqueous solution [28]. This relation between ω_{RBM} and d_t is needed to connect the RRS experiments and the Kataura plot (Fig. 3). This relation also makes connections to prior theoretical works studying the effect of the deformation of the C–C bond angles and bond lengths on ω_{RBM} on other Raman features [34]. However, the connection between the formula $\omega_{RBM} = 248/d_t$, obtained for isolated tubes in the d_t range $1.2 < d_t < 1.6$ nm on a Si/SiO$_2$ substrate and the results given above for small d_t SWNTs still remains to be resolved.

Efforts have been made to observe of the electronic transition energies for light polarized perpendicular to the nanotube axis [35,36]. For SWNT bundle samples, some special RBM spectra have been observed, and these spectra can be explained by a Kataura plot not for E_{ii}, but for $E_{i,i\pm1}$ transitions [12]. This change in the polarization seen by a particular SWNT (suppression of the antenna effect) is attributed to fields from neighboring SWNTs [35]. A general picture corresponding to that shown in Fig. 7b for the $E_{i,i\pm1}$ transitions will be important for gaining a deeper understanding of the electronic properties of SWNTs.

3.4.3. Raman Intensity and Characterization of the (n, m) Population

As the (n, m) dependence of the resonance Raman spectra becomes well established, very important information that can be obtained from RRS is the amount of each specific (n, m) species in a bulk sample and the metal vs. semiconductor population ratio. Such information is very important for advancing both the synthesis and separation processes aimed at producing carbon nanotube samples for applications, depending on their electronic properties.

The method for quantifying the (n, m) population by using resonance Raman scattering is based on the assumption that the intensity for the fully resonant Raman signal depends on the scattering efficiency (or Raman cross-section) of each specific (n, m) nanotube species and its population in the sample. Therefore, by measuring the fully resonant Raman intensity for each specific nanotube in the sample (see Fig. 7a), and by correcting for the (n, m) dependent Raman cross-section for each (n, m), the amount of each (n, m) species in the sample is obtained.

Since the electron–phonon coupling exhibits a strong (n, m) dependence [37], in order to characterize the population of specific (n, m) SWNTs in a sample, the RBM resonance intensities must be analyzed considering the (n, m) dependence of the RBM Raman cross-section. We expect the ratio $P = I_{\mathrm{RBM}}^{\mathrm{EXP}}/I_{\mathrm{RBM}}^{\mathrm{CALC}}$ to give the population P of each specific (n, m) SWNT within the samples. The first-order Raman intensity $I(\omega, E_{\mathrm{laser}})$ as a function of phonon energy, $\hbar\omega$, and incident laser energy, E_{laser} is calculated by [38,39]

$$I(\omega, E_{\mathrm{laser}}) = \sum_j \left| \sum_b \frac{M^d(k-q,jb)M^{\mathrm{ep}}(q,ba)M^d(k,aj)}{\Delta E_{aj}(\Delta E_{aj} - \hbar\omega)} \right|^2 \qquad (4)$$

in which $\Delta E_{aj} \equiv E_{\mathrm{laser}} - (E_a - E_j) - i\gamma$, and j, a, and b denote, respectively, the initial state, the excited states, and the scattered states of an electron, while γ denotes the broadening factor of the resonance event. Such an analysis has been applied to quantify the (n, m) population in SWNTs grown by the so-called CoMoCAT process [40]. This growth process has been considered the most successful in producing samples with a very narrow d_t distribution. By analyzing the P obtained by RRS from CoMoCAT SWNTs [41], it is clear that the semiconducting (6, 5) SWNT is the most abundant species, representing about 2/5 of the sample. By summing up all the

1 *P* for semiconducting and metallic tubes, a S:M ratio of 11:1 is obtained, showing a large dominance of S species in this growth process.

3

3.4.4. Characterization of Environmental Effects

5 Another application of Raman spectroscopy research is to quantify the effect of the SWNT environment on their electronic and vibrational properties. Because of the

7 environment (wrapped by DNA or SDS, bundled, in suspension, or temperature and pressure) seen by a (n, m) SWNT, the E_{ii} values can shift by up to 80 meV. We call

9 these shifts in E_{ii} environmental effects. Effects of the environment generally have a smaller influence on ω_{RBM}.

11 The environment is observed to asymmetrically broaden and even to split the RBM feature observed from one single (n, m) tube wrapped by DNA [42]. The E_{ii} of

13 the SWNT are perturbed by changing the dielectric constant, temperature, and pressure. One illustration of an environmental effect is shown in Fig. 8 where the

15 dependence of the RBM spectra on the laser intensity for a fixed $E_{laser} = 1.72$ eV is shown, indicating that the relative intensities of the RBM peaks change with

17 increasing laser power [28]. The transition energies E_{22}^{S} in Fig. 8b also vary with the laser power density, for each of the eight SWNTs with (n, m) assignments in Fig. 8a.

19 Here the E_{22}^{S} move in opposite directions when the laser power increases for S SWNTs of the MOD1 type (dotted lines) and of the MOD2 type (solid lines). The

21 E_{22}^{S} undergo a downshift for MOD1 SWNTs and an upshift for MOD2 SWNTs (similar to the recently reported uniaxial strain-enhanced effect observed in SWNT
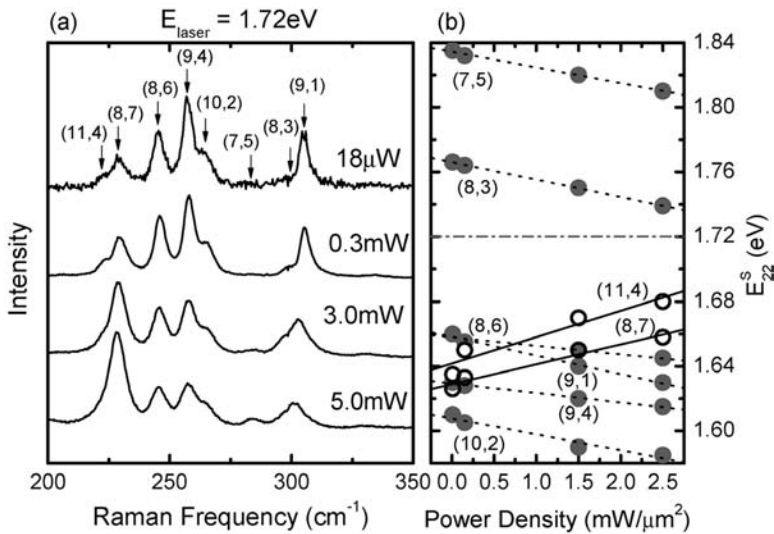
23

Fig. 8. (a) Dependence of the RBM spectra for HiPco SWNTs in bundles on the laser excitation power for a fixed $E_{laser} = 1.72$ eV. (b) Dependence of the transition energies E_{22}^{S} on the laser power density for specific (n, m) SWNTs. Gray dots and open circles are for MOD1 and MOD2 nanotubes, respectively.

bundles [43]), thus explaining the changes in the relative intensities for the RBM peaks observed from a single E_{laser} (Fig. 8a). The changes in E_{ii} due to sample heating show that control of the laser power is important when analyzing the RRS of a nanotube sample.

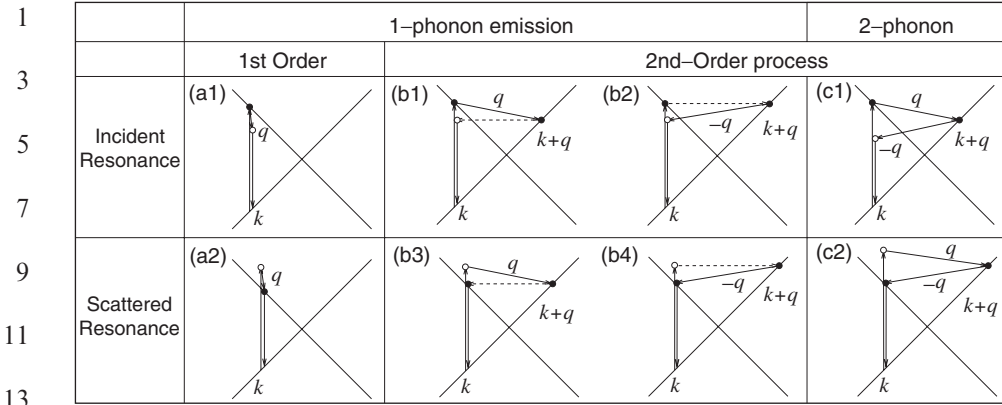### 3.5. Double Resonance Second-Order and Defect-Induced Modes

Many features in addition to the RBM and G-band features are also observed in the Raman spectra in Fig. 1. In this section we focus our attention on defect-induced modes and double resonance (DR) second-order features. Of these, the so-called D band (around 1200–1400 cm^{-1}) is the most extensively studied feature [44] and is a well-known example of a disorder-induced band, that has been widely used to characterize disorder in many kinds of graphitic materials [45], including SWNTs. Furthermore, a rich set of spectral features is observed for the intermediate frequency range between 600 and 1100 cm^{-1} [46], and several multi-phonon bands can be observed above 1700 cm^{-1} [47], the best known being the so-called G'-band (overtone of the D band) observed in the range 2400–2800 cm^{-1} [47,48].

In general, the observation of overtones and combination modes in condensed matter systems is rare because of dispersion effects which make these features too weak and broad to pick out from the noisy background. The enhanced intensity caused by the DR process in graphite-like materials and the intensity enhancement caused by the vHSs in SWNTs, however, allow such overtones and combination modes to be quite clearly observed. These DR features usually exhibit changes in their excited electronic states with changing E_{laser}, thereby providing new information about SWNT properties. To understand the physics related to overtones and combination modes, the basic physics for higher order scattering events for SWNTs are discussed here.

3.5.1. Double Resonance Scattering
In second-order Raman scattering (see Fig. 9b and c), the $\mathbf{q}$ and $-\mathbf{q}$ scattering wave vectors are involved, so that an electron can return to its original k position after scattering. Second-order Raman scattering consists of either (b) one-phonon and one-elastic scattering event, or (c) two-phonon scattering events. In the case of two-phonon scattering events, we can have involvement of either the same phonon modes (overtone mode) or different phonon modes (combination modes).

In second-order DR processes for carbon materials (see Fig. 9b and c), the electron (1) absorbs a photon at a $\mathbf{k}$ state, (2) scatters to $\mathbf{k} + \mathbf{q}$ states, (3) scatters back to a $\mathbf{k}$ state, and (4) emits a photon by recombining with a hole at a $\mathbf{k}$ state. The two scattering processes consist of either elastic scattering by the defects of the crystal or inelastic scattering by emitting a phonon, as shown in Fig. 9. Thus (1) one-elastic and one-inelastic scattering event (Fig. 9b) and (2) two-inelastic scattering events (Fig. 9c) are relevant to 2nd order Raman spectroscopy. Hereafter we call them, respectively, one-phonon and two-phonon DR Raman spectra [49]. In a DR Raman process, two resonance conditions for three intermediate states should be satisfied, in which the intermediate $\mathbf{k} + \mathbf{q}$ state is always a real electronic state (solid circles in

	1–phonon emission			2–phonon
	1st Order	2nd–Order process		
Incident Resonance	(a1) q k	(b1) q $k+q$ k	(b2) $-q$ $k+q$ k	(c1) q $-q$ $k+q$ k
Scattered Resonance	(a2) q k	(b3) q $k+q$ k	(b4) $-q$ $k+q$ k	(c2) q $-q$ $k+q$ k

Fig. 9. (a) First-order and (b) one-phonon second-order, (c) two-phonon second-order, resonance Raman spectral processes: (top) incident photon resonance and (bottom) scattered photon resonance conditions. For one-phonon, second-order transitions, one of the two scattering events is an elastic scattering event (dashed lines). Resonance points are shown as solid circles. See text for details.

Fig. 9) and either the initial or the final k states is a real electronic state. The Raman intensity of a DR process is, in principle, comparable to that of a first-order process obeying a single resonance condition. In order to satisfy energy–momentum conservation in one-phonon DR Raman spectroscopy (see Fig. 9b1 and b2), the inelastic scattering process gives a shorter phonon $\mathbf{q}$ vector from the initial $\mathbf{k}$ state than the elastic scattering process.

The electronic structure of 2D graphite near the Fermi energy E_F is linear in wave vector $\mathbf{k}$, which is expressed by the crossed solid lines in Fig. 9. The crossing point corresponds to E_F located at the K point. When the laser energy E_{laser} increases, the resonance k vector for the electron moves away from the K point. In the DR process, the corresponding $\mathbf{q}$ vector for the phonon increases with increasing $\mathbf{k}$, measured from the K point. Thus by changing E_{laser}, we can observe the phonon energy $\hbar\omega(q)$ along the phonon dispersion relations (Fig. 10). This effect is observed experimentally as a dispersion of the phonon energy as a function of E_{laser} [49]. A tunable laser system can directly measure this dispersive behavior for a dispersive feature, such as the D-band or the G'-band in the Raman spectrum (see Fig. 1).

When we consider the energy and momentum conservation for $\mathbf{k}$ and $\mathbf{q}$, we need to introduce two other concepts to describe the scattering processes: intravalley and intervalley scattering, respectively, associated with $\mathbf{q} = 0$ and $\mathbf{q} = 2\mathbf{k}$ phonons where the value of $\mathbf{k}$ is measured from the K (or K') point [50,51]. Since E_F is located at two inequivalent K and K' points in the 2D Brillouin zone, we can consider the scattering not only in the vicinity of K (or K'), as shown in Fig. 9, but also in scattering from K to K' (or from K' to K). The corresponding $\mathbf{q}$ vector for intravalley and intervalley scattering is, respectively, near the Γ and K points, as measured from the Γ point. Only $\mathbf{q} = 2\mathbf{k}$ modes show a large dispersive behavior for the Raman frequency vs. E_{laser}.
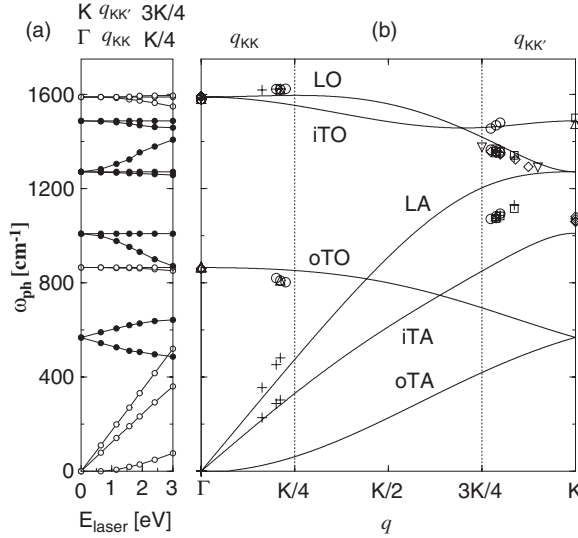
Fig. 10. (a) Calculated Raman frequencies for the double resonance (DR) condition vs. E_{laser} (bottom axis) and vs. q vector along $\Gamma-K$ (top axis). Solid and open circles correspond to phonon modes near the K and Γ points, respectively. (b) The six graphite phonon dispersion curves (lines) and experimental Raman data (symbols) [50].

Both in graphite and in SWNTs, the D-band at $1350\,\text{cm}^{-1}$ and the G'-band at $2700\,\text{cm}^{-1}$ (for $E_{laser} = 2.41\,\text{eV}$) are, respectively, due to one-phonon and two-phonon, 2nd order Raman intervalley scattering processes. Thus for graphite, the D-band spectra appearing at $1350\,\text{cm}^{-1}$ (one-phonon DR) can be fitted to two Lorentzians, while the G'-band feature at $2700\,\text{cm}^{-1}$ (two-phonon DR) can be fitted to one Lorentzian [51]. The disorder-induced D band is observed in disordered graphite-like materials, including carbon nanotubes, while its second-order harmonic, the G'-band is observed even in the absence of defects. Typically ω_D and $\omega_{G'}$ would be measured for $E_{laser} = 2.41\,\text{eV}$ and their dispersion would be $53\,\text{cm}^{-1}/\text{eV}$ and $106\,\text{cm}^{-1}/\text{eV}$, respectively, for SWNTs. Although the ω_D and $\omega_{G'}$ dependences on E_{laser} are linear for most disordered graphite-like materials, ω_D and $\omega_{G'}$ in SWNTs exhibit an anomalous oscillatory dispersive effect, since the resonance condition for SWNTs occur at their 1D vHSs [48,52,53].

Many weak features in the Raman spectra for SWNTs can be assigned to one-phonon or two-phonon, 2nd order DR processes. These are listed in Table 1 together with their frequencies and dispersion $d\omega/dE_{laser}$. Also of importance is the variation of their mode frequencies with tube diameter d_t [54].

3.5.2. Characterizing Doping from the D and G' bands

The D and G' bands provide a sensitive tool for characterizing carbon nanotube defects, functionalization, and doping [8,9]. While high resolution TEM and EELS AU:2 techniques were not sensitive enough to detect boron in SWNTs, such doping could

Table 1. Properties of the various Raman features in graphite and SWNTs[a].

Name	ω (cm^{-1})	Res.[b]	$d\omega/dE$[c]	Notes
iTA	288	DR1-AV	129	iTA mode, $\mathbf{q} = 2\mathbf{k}$
LA	453	DR1-AV	216	LA mode, $\mathbf{q} = 2\mathbf{k}$
RBM	$248/d_t$	SR	0	Nanotube only, vibration of radius
oTO	860	DR1-AV	0	IR-active mode in graphite
D	1350	DR1-EV	53	LO or iTO mode, $\mathbf{q} = 2\mathbf{k}$
LO	1450	DR1-EV	0	LO mode, $\mathbf{q} = 0$
G	1582	SR	0	Raman-active mode of graphite
M^-	1732	DR2-AV	-26	Overtone of oTO mode, $\mathbf{q} = 2\mathbf{k}$
M^+	1755	DR2-AV	0	Overtone of oTO mode, $\mathbf{q} = 0$
iTOLA	1950	DR2-AV	230	Combinational mode of iTO and LA
G'	2700	DR2-EV	106	Overtone of D mode
2LO	2900	DR2-AV	0	Overtone of LO mode
2G	3180	DR2-AV	0	Overtone of G mode

[a]Dispersive mode frequencies ω are given at $E_{laser} = 2.41$ eV.
[b]The notation used here to classify resonance Raman scattering processes is: SR: 1st order, single resonance; DR1: 1 phonon, double resonance; DR2: 2 phonon, double resonance. AV: intravalley scattering; EV: intervalley scattering.
[c]$d\omega/dE$ denotes the change ω in cm^{-1} produced by changing $E = E_{laser}$ by 1 eV.

be detected in their Raman spectra taken for B concentrations up through 3 at.% B in the target. The effect of doping MWNTs (multiwall carbon nanotubes) and SWNTs of large and small d_t, is observed as an increase in the intensity of the disorder-induced *D*-band in the Raman spectra [55–57]. Upon boron doping, the *D*-band intensity increases for higher doping levels [56,57], and in addition other changes to the spectra occur (see Fig. 11), such as bringing the RBM feature into better resonance with E_{laser} by shifting E_{ii} values and bringing more semiconducting tubes into resonance as can be seen in Fig. 11 by the change in the *G'*-band lineshape. Furthermore, ω_D and $\omega_{G'}$ are observed to downshift with boron doping, consistent with an increase in the in-plane lattice constant and a weakening of the B–C in-plane bond strength relative to that of the C–C bond, which is also observed in boron doped graphite [58]. One remarkable effect is a relatively larger downshift observed in $\omega_{G'}$ for metallic SWNTs compared to semiconducting SWNTs because of the larger occupation of states at E_F in M SWNTs. Thus the effect of hole addition through boron doping moves down E_F slightly from approximately mid-gap, in contrast to S SWNTs for which E_F drops all the way down to the highest lying vHS in the valence band.

3.5.3. Other Double Resonance Features

Interesting examples of overtone features are the features between 1700 and 2100 cm^{-1} shown in Fig. 12a, for SWNT bundles [47] and for several laser lines (E_{laser}). The two features near 1740 cm^{-1} (*M* band) are attributed to overtones of the out-of-plane (oTO), infrared-active mode at 867 cm^{-1} in graphite. Here the M^+ feature is identified with a nondispersive (intravalley $\mathbf{q} = 0$ scattering) DR process, and the M^- with a dispersive (intervalley $\mathbf{q} = 2b$) DR process (see Fig. 12a) [47]. The
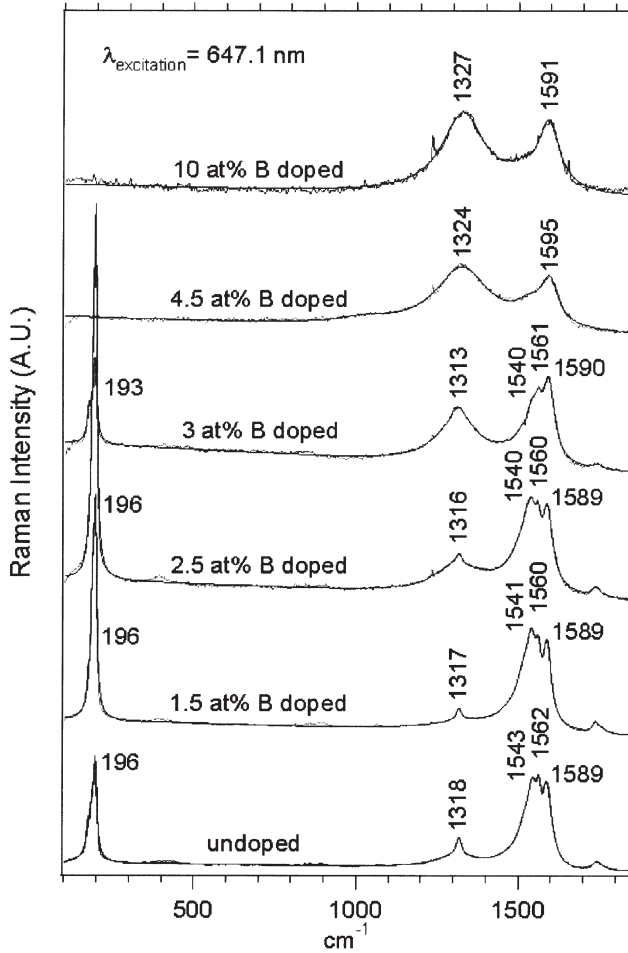
Fig. 11. First-order room temperature Raman spectra of SWNT bundle samples generated from targets with the indicated boron concentrations. All Raman spectra were excited using $E_{laser} = 1.96$ eV (647.1 nm) excitation energy. The spectra for the 4.5 and 10 at.% samples correspond to spectra for disordered graphite [57].

second-order *M*-band features are also interesting as an example of an overtone mode near $\mathbf{q} = 0$ whose fundamental (oTO) is not Raman-active (but is IR active) in the first-order spectrum of graphite, but can be observed in second order through the DR process. The *M*-band modes are further enhanced in SWNTs by van Hove singularity effects, and by symmetry-breaking effects associated with SWNT curvature.

The iTOLA, assigned as a combination mode not seen in graphite, is a highly dispersive DR-derived mode, upshifting from 1864 to 2000 cm^{-1} as E_{laser} varies from 1.58 to 2.71 eV [47]. To account for its large observed dispersion with E_{laser},
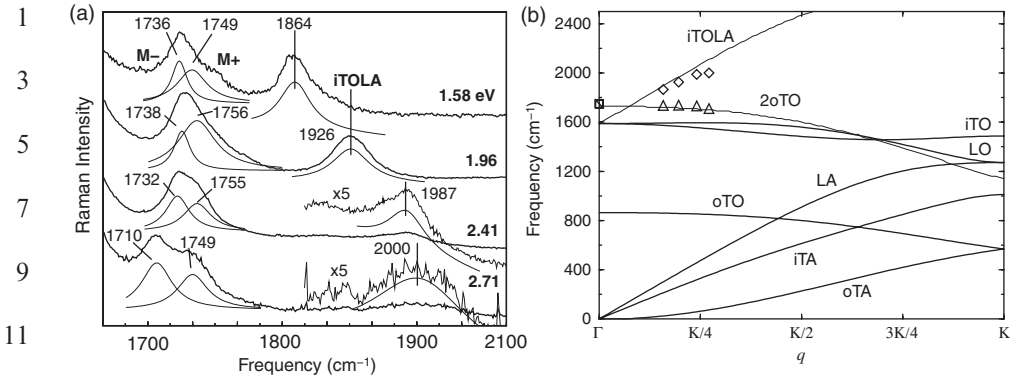
Fig. 12. (a) Lorentzian fits of the Raman spectra taken at several E_{laser} values for the *M*-bands near $1750\,cm^{-1}$ and the highly dispersive iTOLA feature observed at $1950\,cm^{-1}$ in SWNT bundles [47,59]. (b) Phonon dispersion for 2D graphite along the $\Gamma - K$ direction, including the dispersion for 2oTO (*M*-band) and iTO + LA (iTOLA). Squares, up-triangles, and diamonds denote experimental values for the *M* ($q = 0$ and $q = 2k$) and iTOLA ($q = 2k$) bands [47].

this so-called iTOLA band is attributed to a combination of two intravalley phonons, iTO + LA, one from the in-plane transverse optical branch (iTO) and the second phonon from the longitudinal acoustic (LA) branch, where the acoustic LA phonon is responsible for the large dispersion (see Fig. 12a) that is observed experimentally [47]. Fig. 12b shows the relation of the iTOLA mode dispersion to phonon branches in 2D graphite.

3.5.4. Step-Like Behavior of Dispersive Raman Spectra
From 700 to $1100\,cm^{-1}$, strongly dispersive Raman spectra are found for the so-called intermediate frequency modes (IFM) in tube bundle samples [60]. Fig. 13a plots the E_{laser} dependence of the IFM features shown in Fig. 13b for four E_{laser} values [46]. Interestingly, the use of a tunable laser system with a small energy spacing between E_{laser} lines, brings into focus a new and very unusual effect for Raman spectroscopy in general. When E_{laser} is varied, individual Raman peaks first increase and then decrease in intensity, while remaining approximately constant in phonon frequency. This behavior can be seen clearly by observing some of the well-resolved sharp peaks (see arrows in Fig. 13a). The dispersive behavior is not monotonic, as observed for many features in graphite-like materials due to energy-selective DR Raman scattering processes [50,61], but the dispersive behavior rather occurs in "steps."

In the 2D graphite parent material, the IFM spectral region contains an out-of-plane (o) optical (O) branch, with $\omega_O(q = 0)$ approximately $860\,cm^{-1}$ for the oTO mode and by acoustic (A) branches [10]. In a second-order scattering process, these modes can become Raman-active, and the sum and difference of phonon frequencies can be observed. Such an effect is common in molecular spectroscopy, but is very unusual for solid state spectroscopy, where too many combinations are possible, and
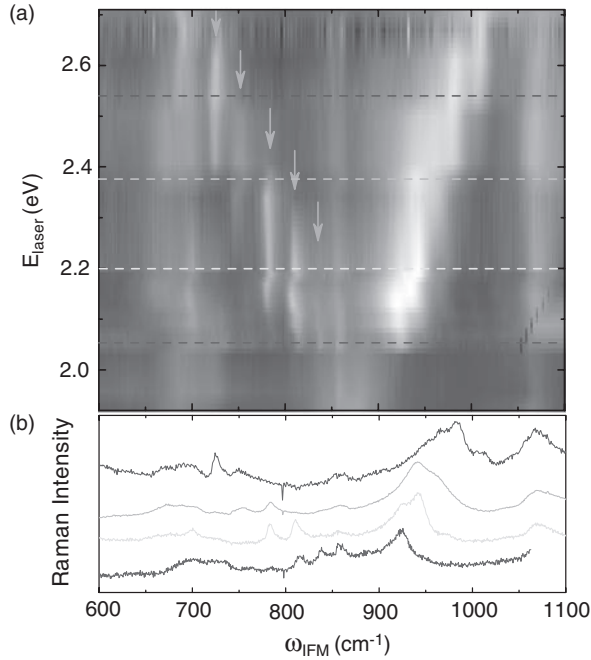
1

3

5

7

9

11

13

15

17

19

21

23 *Fig. 13.* (a) Two-dimensional plot for the E_{laser} dependence for the Raman spectra of
SWNT bundles in the IFM range. The illuminated areas indicate high Raman intensity.
25 Arrows point to five well-defined ω_{IFM}^{-} features. (b) IFM Raman spectra with $E_L = 2.05$
(top), 2.20, 2.34, and 2.54 eV (bottom) [46].

27

the averaging over many wave vector-allowed processes gives rise to just a broad
29 background rather than to observable peaks with well-defined frequencies. The
IFMs in SWNTs arise from such an effect and can be related to a vHS for each
31 (n, m) SWNT and to the combination of two phonons, one optical and one acoustic
to give the sum $\omega_{IFM}^{+} = \omega_O + \omega_A$ (creation of two phonons) and the difference
33 $\omega_{IFM}^{-} = \omega_O - \omega_A$ (creation of an O phonon and the annihilation of an A phonon).
The ω_{IFM}^{+} and ω_{IFM}^{-} thus give rise to the positively and negatively dispersive IFMs
35 shown in Fig. 13a, respectively.

37

4. SUMMARY

39

Each of the many spectral features appearing in the Raman spectra of SWNTs
41 provide important characterization information about SWNTs, with complementary
information provided by ensembles of SWNTs in SWNT bundle samples and by
43 isolated (n, m) SWNTs at the single nanotube level. Emphasis is given both to Raman
spectroscopy for 1D systems and to the use of Raman spectroscopy to characterize
45 the (n, m) structure, defects, and the various environmental effects encountered by

SWNTs. Raman spectroscopy is also closely connected to PL spectroscopy of semiconducting SWNTs, since both experimental techniques are strongly sensitive to the transition energies of individual SWNTs, to their electronic density of states, and to their interactions. Combination of transport and other experiments with Raman spectroscopy will be highly desirable to further our understanding of the electronic and vibrational structure of SWNTs.

NOTE

1. A CVD grown sample from high purity CO gas.

ACKNOWLEDGMENTS

REFERENCES

[1] A.M. Rao, E. Richter, S. Bandow, B. Chase, P.C. Eklund, K.W. Williams, S. Fang, K.R. Subbaswamy, M. Menon, A. Thess, R.E. Smalley, G. Dresselhaus and M.S. Dresselhaus, Diameter-selective Raman scattering from vibrational modes in carbon nanotubes, *Science* **275**, AU :3 187–191 (1997).

[2] A. Jorio, R. Saito, J.H. Hafner, C.M. Lieber, M. Hunter, T. McClure, G. Dresselhaus and M.S. Dresselhaus, Structural (*n*, *m*) determination of isolated single-wall carbon nanotubes by resonant Raman scattering, *Phys. Rev. Lett.* **86**, 1118–1121 (2001).

[3] J.M. Holden, P. Zhou, X.-X. Bi, P.C. Eklund, S. Bandow, R.A. Jishi, K. Das Chowdhury, G. Dresselhaus and M.S. Dresselhaus, Raman scattering from nanoscale carbons generated in a cobalt-catalyzed carbon plasma, *Chem. Phys. Lett.* **220**, 186–191 (1994).

[4] K. Tohji, T. Goto, H. Takahashi, Y. Shinoda, N. Shimizu, B. Jeyadevan, I. Matsuoka, Y. Saito, A. Kasuya, T. Ohsuna, K. Hiraga and Y. Nishina, Purifying single walled nanotubes, *Nature* **383**, 679 (1996).

[5] M.S. Dresselhaus, G. Dresselhaus, A.M. Rao, A. Jorio, A.G. Souza Filho, Ge.G. Samsonidze and R. Saito, Resonant Raman scattering on one-dimensional systems, *Indian J. Phys.* **77B**, 75–99 (2003).

[6] S. Iijima and T. Ichihashi, Single shell carbon nanotubes of 1-nm diameter, *Nature (Lond.)* **363**, 603 (1993).

[7] D.S. Bethune, C.H. Kiang, M.S. de Vries, G. Gorman, R. Savoy, J. Vazquez and R. Beyers, Cobalt-catalysed growth of carbon nanotubes with single atomic layer walls, *Nature (Lond.)* **363**, 605 (1993).

[8] M.S. Dresselhaus, G. Dresselhaus, A. Jorio, A.G. Souza Filho and R. Saito, Raman spectroscopy on isolated single wall carbon nanotubes, *Carbon* **40**, 2043–2061 (2002).

[9] M.S. Dresselhaus, G. Dresselhaus, R. Saito and A. Jorio, Raman spectroscopy of carbon nanotubes, *Phys. Rep.* **409**, 47–99 (2005).

[10] R. Saito, G. Dresselhaus and M.S. Dresselhaus, *Physical Properties of Carbon Nanotubes* (Imperial College Press, London, 1998).

[11] Ge.G. Samsonidze, R. Saito, A. Jorio, M.A. Pimenta, A.G. Souza Filho, A. Grüneis, G. Dresselhaus and M.S. Dresselhaus, The concept of cutting lines in carbon nanotube science, *J. Nanosci. Nanotechnol.* **3**, 431–458 (2003).

[12] H. Ajiki and T. Ando, Aharonov–Bohm effect in carbon nanotubes, *Physica B Condens. Matter* **201**, 349 (1994).

[13] H. Ajiki and T. Ando, Carbon nanotubes: Optical absorption in Aharonov–Bohm flux, *Jpn. J. Appl. Phys. Suppl.* **34-1**, 107–109 (1995).

[14] H. Kataura, Y. Kumazawa, N. Kojima, Y. Maniwa, I. Umezu, S. Masubuchi, S. Kazama, X. Zhao, Y. Ando, Y. Ohtsuka, S. Suzuki, and Y. Achiba, in *Proceedings of the International Winter School on Electronic Properties of Novel Materials (IWEPNM'99)*, American Institute of Physics, Woodbury, NY, 1999, AIP Conference Proceedings, 486 (1999) pp. 328–332.

[15] R. Saito, G. Dresselhaus and M.S. Dresselhaus, Trigonal warping effect of carbon nanotubes, *Phys. Rev. B* **61**, 2981–2990 (2000).

[16] Ge.G. Samsonidze, A. Grüneis, R. Saito, A. Jorio, A.G. Souza Filho, G. Dresselhaus and M.S. Dresselhaus, Interband optical transitions in left-, right-handed single-wall carbon nanotubes, *Phys. Rev. B* **69**, 205402(1)–205402(11) (2004).

[17] R. Saito, M. Fujita, G. Dresselhaus and M.S. Dresselhaus, Electronic structures of carbon fibers based on C_{60}, *Phys. Rev. B* **46**, 1804–1811 (1992).

[18] A. Jorio, C. Fantini, M.A. Pimenta, R.B. Capaz, Ge.G. Samsonidze, G. Dresselhaus, M.S. Dresselhaus, J. Jiang, N. Kobayashi, A. Grüneis and R. Saito, Resonance Raman spectroscopy (n, m) dependent effects in small diameter single-wall carbon nanotubes, *Phys. Rev. B* **71**, 075401 (2005).

[19] S.M. Bachilo, M.S. Strano, C. Kittrell, R.H. Hauge, R.E. Smalley and R.B. Weisman, Structure-assigned optical spectra of single walled carbon nanotubes, *Science* **298**, 2361–2366 (2002).

[20] R.B. Weisman and S.M. Bachilo, Dependence of optical transition energies on structure for single-walled carbon nanotubes in aqueous suspension: An empirical Kataura plot, *Nanoletters* **3**, 1235–1238 (2003).

[21] A. Jorio, A.G. Souza Filho, G. Dresselhaus, M.S. Dresselhaus, R. Saito, J.H. Hafner, C.M. Lieber, F.M. Matinaga, M.S.S. Dantas and M.A. Pimenta, Joint density of electronic states for one isolated single-wall carbon nanotube studied by resonant Raman scattering, *Phys. Rev. B* **63**, 245416-1–245416-4 (2001).

[22] A. Jorio, A.G. Souza Filho, G. Dresselhaus, M.S. Dresselhaus, A.K. Swan, M.S. Ünlü, B. Goldberg, M.A. Pimenta, J.H. Hafner, C.M. Lieber and R. Saito, G-band resonant Raman study of 62 isolated single wall carbon nanotubes, *Phys. Rev. B* **65**, 155412 (2002).

[23] A. Jorio, A.G. Souza Filho, V.W. Brar, A.K. Swan, M.S. Ünlü, B.B. Goldberg, A. Righi, J.H. Hafner, C.M. Lieber, R. Saito, G. Dresselhaus and M.S. Dresselhaus, Polarized resonant Raman study of isolated single-wall carbon nanotubes: Symmetry selection rules, dipolar, multipolar antenna effects, *Phys. Rev. B Rapid* **65**, R121402 (2002).

[24] A. Jorio, M.A. Pimenta, A.G. Souza Filho, Ge.G. Samsonidze, A.K. Swan, M.S. Ünlü, B.B. Goldberg, R. Saito, G. Dresselhaus and M.S. Dresselhaus, Resonance Raman spectra of carbon nanotubes by cross-polarized light, *Phys. Rev. Lett.* **90**, 107403 (2003).

[25] A. Jorio, G. Dresselhaus, M.S. Dresselhaus, M. Souza, M.S.S. Dantas, M.A. Pimenta, A.M. Rao, R. Saito, C. Liu and H.M. Cheng, Polarized Raman study of single-wall semiconducting carbon nanotubes, *Phys. Rev. Lett.* **85**, 2617–2620 (2000).

[26] G.S. Duesberg, I. Loa, M. Burghard, K. Syassen and S. Roth, Polarized Raman spectroscopy on isolated single-wall carbon nanotubes, *Phys. Rev. Lett.* **85**, 5436–5439 (2000).

[27] Y. Wang, K. Kempa, B. Kimball, J.B. Carlson, G. Benham, W.Z. Li, T. Kempa, J. Rybczynski, A. Herczynski and Z.F. Ren, Receiving and transmitting light-like radio waves: Antenna effect in arrays of aligned carbon nanotube, *Appl. Phys. Lett.* **85**, 2607 (2004).

[28] C. Fantini, A. Jorio, M. Souza, A.J. Mai, Jr., M.S. Strano, M.S. Dresselhaus and M.A. Pimenta, Optical transition energies, radial breathing modes for HiPco carbon nanotubes from Raman spectroscopy, *Phys. Rev. Lett.* **93**, 147406 (2004).

[29] Ge.G. Samsonidze, R. Saito, N. Kobayashi, A. Grüneis, J. Jiang, A. Jorio, S.G. Chou, G. Dresselhaus and M.S. Dresselhaus, Family behavior of the optical transition energies in single-wall carbon nanotubes of smaller diameters, *Appl. Phys. Lett.* **85**, 5703–5705 (2004).

[30] H. Kataura, Y. Kumazawa, Y. Maniwa, I. Umezu, S. Suzuki, Y. Ohtsuka and Y. Achiba, Optical properties of single-wall carbon nanotubes, *Synth. Metals* **103**, 2555–2558 (1999).

[31] S.D.M. Brown, A. Jorio, P. Corio, M.S. Dresselhaus, G. Dresselhaus, R. Saito and K. Kneipp, Origin of the Breit–Wigner–Fano lineshape of the tangential G-band feature of metallic carbon nanotubes, *Phys. Rev. B* **63**, 155414 (2001).

[32] M.A. Pimenta, A. Marucci, S. Empedocles, M. Bawendi, E.B. Hanlon, A.M. Rao, P.C. Eklund, R.E. Smalley, G. Dresselhaus and M.S. Dresselhaus, Raman modes of metallic carbon nanotubes, *Phys. Rev. B Rapid* **58**, R16016–R16019 (1998).

[33] M.J. O'Connell, S.M. Bachilo, X.B. Huffman, V.C. Moore, M.S. Strano, E.H. Haroz, K.L. Rialon, P.J. Boul, W.H. Noon, C. Kittrell, J. Ma, R.H. Hauge, R.B. Weisman and R.E. Smalley, Band gap fluorescence from individual single walled carbon nanotubes, *Science* **297**, 593–596 (2002).

[34] J. Kürti, V. Zólyomi, M. Kertesz and G.Y. Sun, The geometry, the radial breathing mode of carbon nanotubes: Beyond the ideal behaviour, *New J. Phys.* **5** (2003) Art. 125

[35] A. Grüneis, R. Saito, J. Jiang, Ge.G. Samsonidze, M.A. Pimenta, A. Jorio, A.G. Souza Filho, G. Dresselhaus and M.S. Dresselhaus, Resonant Raman spectra of carbon nanotube bundles observed by perpendicularly polarized light, *Chem. Phys. Lett.* **387**, 301–306 (2004).

[36] S. Maruyama, A molecular dynamics simulation of heat conduction of a finite length single-walled carbon nanotube, *Microscale Thermophys. Eng.* **7**, 41–50 (2003).

[37] J. Jiang, R. Saito, A. Grüneis, S.G. Chou, Ge.G. Samsonidze, A. Jorio, G. Dresselhaus, and M.S. Dresselhaus, Resonance Raman intensity excitation spectra of single-wall carbon nanotubes, *Phys. Rev. B* (2005), in press. AU :4

[38] M. Cardona, vol., 50, pp. 19–176, chapter 2 (Topics in Applied Physics). AU :5

[39] R.M. Martin and L.M. Falicov, vol., 8, pp. 79–145, chapter 3 (Topics in Applied Physics).

[40] B. Kitiyanan, W.E. Alvarez, J.H. Harwell and D.E. Resasco, Controlled production of single-wall carbon nanotubes by catalytic decomposition of Co on bimetallic Co–Mo catalysts, *Chem. Phys. Lett.* **317**, 497–503 (2000).

[41] A. Jorio et al. (unpublished). AU :6

[42] A. Jorio, C. Fantini, L.G. Cançado, H.B. Ribeiro, A.P. Santos, C.A. Furtado, M.S. Dresselhaus, G. Dresselhaus, Ge.G. Samsonidze, A. Grüneis, J. Jiang, N. Kobayasi, R. Saito, and M.A. Pimenta, in *Proceedings of the XVIII International Winter School on the Electronic Properties of Novel Materials*, pp. (Kirchberg Winter School, Austria). AU :7

[43] M. Lucas and R.J. Young, Effect of uniaxial strain deformation upon the Raman radial breathing modes of single-wall carbon nanotubes in composites, *Phys. Rev. B* **69**, 085405 (2004).

[44] M.J. Matthews, M.A. Pimenta, G. Dresselhaus, M.S. Dresselhaus and M. Endo, Origin of dispersive effects of the Raman *D*-band in disordered carbon materials, *Phys. Rev. B* **59**, R6585–R6588 (1999).

[45] M.S. Dresselhaus and R. Kalish, *Ion Implantation in Diamond, Graphite and Related Materials*, vol. 22 (Springer-Verlag, Berlin, 1992); [Springer Series in Materials Science].

[46] C. Fantini, A. Jorio, M. Souza, L.O. Ladeira, M.A. Pimenta, A.G. Souza Filho, R. Saito, Ge.G. Samsonidze, G. Dresselhaus and M.S. Dresselhaus, One-dimensional character of combination modes in the resonance Raman scattering of carbon nanotubes, *Phys. Rev. Lett.* **93**, 087401 (2004).

[47] V.W. Brar, Ge.G. Samsonidze, G. Dresselhaus, M.S. Dresselhaus, R. Saito, A.K. Swan, M.S. Ünlü, B.B. Goldberg, A.G. Souza Filho and A. Jorio, Second-order harmonic, combination modes in graphite, single-wall carbon nanotube bundles, isolated single-wall carbon nanotubes, *Phys. Rev. B* **66**, 155418 (2002).

[48] M.A. Pimenta, E.B. Hanlon, A. Marucci, P. Corio, S.D.M. Brown, S.A. Empedocles, M.G. Bawendi, G. Dresselhaus and M.S. Dresselhaus, The anomalous dispersion of the disorder-induced, the second-order Raman bands in carbon nanotubes, *Braz. J. Phys.* **30**, 423–427 (2000).

[49] R. Saito, A. Grüneis, Ge.G. Samsonidze, V.W. Brar, G. Dresselhaus, M.S. Dresselhaus, A. Jorio, L.G. Cançado, C. Fantini, M.A. Pimenta and A.G. Souza Filho, Double resonance Raman spectroscopy of single wall carbon nanotubes, *New J. Phys.* **5**, 157.1–157.15 (2003).

[50] R. Saito, A. Jorio, A.G. Souza Filho, G. Dresselhaus, M.S. Dresselhaus and M.A. Pimenta, Probing phonon dispersion relations of graphite by double resonance Raman scattering, *Phys. Rev. Lett.* **88**, 027401 (2002).

[51] L.G. Cançado, M.A. Pimenta, R. Saito, A. Jorio, L.O. Ladeira, A. Grüneis, A.G. Souza Filho, G. Dresselhaus and M.S. Dresselhaus, Stokes, anti-Stokes double resonance Raman scattering in two-dimensional graphite, *Phys. Rev. B* **66**, 035415 (2002).

[52] S.D.M. Brown, A. Jorio, G. Dresselhaus and M.S. Dresselhaus, The *D*-band feature of carbon nanotubes, *Phys. Rev. B* **64**, 073403 (2001).

[53] A. Grüneis, M. Hulman, Ch. Kramberger, H. Peterlik, H. Kuzmany, H. Kataura, and Y. Achiba, in *Proceeding of the International Winter School on Electronic Properties of Novel Materials*, vol. 591, p. 319, AIP Conference Proceedings (2001).

[54] A.G. Souza Filho, A. Jorio, Ge.G. Samsonidze, G. Dresselhaus, M.A. Pimenta, M.S. Dresselhaus, A.K. Swan, M.S. Ünlü, B.B. Goldberg and R. Saito, Competing spring constant versus double resonance effects on the properties of dispersive modes in isolated single wall carbon nanotubes, *Phys. Rev. B* **67**, 035427-1–035427-7 (2003).

[55] W.K. Hsu, S. Firth, P. Redlich, M. Terrones, H. Terrones, Y.Q. Zhu, N. Grobert, A. Schilder, R.J.H. Clark, H.W. Kroto and D.R.M. Walton, Boron-doping effects in carbon nanotubes, *J. Mater. Chem. Lett.* **10**, 1425–1429 (2000).

[56] J. Maultzsch, S. Reich, C. Thomsen, H.S. Webster, R. Czerw, D.L. Carroll, S.M.C. Vieira, P.R. Birkett and C.A. Rego, Raman characterization of boron-doped multiwalled carbon nanotubes, *Appl. Phys. Lett.* **81**, 2647–2649 (2002).

[57] K. McGuire, N. Gothard, P.L. Gai, M.S. Dresselhaus, G. Sumanasekera and A.M. Rao, Synthesis, Raman characterization of boron-doped single walled carbon nanotubes, *Carbon* **43**, 219–227 (2005).

[58] B.T. Kelly, Physics of graphite, *Appl. Sci.* (*Lond.*) (1981).

[59] S.D.M. Brown, P. Corio, A. Marucci, M.A. Pimenta, M.S. Dresselhaus and G. Dresselhaus, Second-order resonant Raman spectra of single-walled carbon nanotubes, *Phys. Rev. B* **61**, 7734–7742 (2000).

[60] L. Alvarez, A. Righi, T. Guillard, S. Rols, E. Anglaret, D. Laplaze and J.-L. Sauvajol, Resonant Raman study of the structure and electronic properties of SWNTs, *Chem. Phys. Lett.* **316**, 186–190 (2000).

[61] C. Thomsen and S. Reich, Double resonant Raman scattering in graphite, *Phys. Rev. Lett.* **85**, 5214 (2000).

AU :8

AUTHOR QUERY FORM

ELSEVIER	**Book: CCMS-V003** **Chapter: 4**	**Please eail or fax your responses and any corrections to:** **Eail:** **Fax:**

Dear Author,

During the preparation of your manuscript for typesetting, some questions may have arisen. These are listed below. Please check your typeset proof carefully and mark any corrections in the margin of the proof or compile them as a separate list*.

Disk use

Sometimes we are unable to process the electronic file of your article and/or artwork. If this is the case, we have proceeded by:

☐ Scanning (parts of) your article   ☐ Rekeying (parts of) your article
☐ Scanning the artwork

Bibliography

If discrepancies were noted between the literature list and the text references, the following may apply:

☐ The references listed below were noted in the text but appear to be missing from your literature list. Please complete the list or remove the references from the text.
☐ *Uncited references:* This section comprises references that occur in the reference list but not in the body of the text. Please position each reference in the text or delete it. Any reference not dealt with will be retained inthis section

Queries and/or remarks

Location in Article	Query / remark	Response
AU:1	As per the style, please provide the abstract.	
AU:2	Please check whether at.% stands for atomic percent in the following sentence: "While high resolution TEM.in the target."	
AU:3	The journal refs. in the reference list contain both the first and last page nos. or only the first page no. Please check.	
AU:4	Please provide the vol. and page no. in the Refs. 37 and 58.	
AU:5	Please provide complete details of the Refs. 38 and 39.	
AU:6	Please provide complete details of Ref. 41 if possible.	
AU:7	Please provide the page range in Ref. 42.	
AU:8	Please provide the venue of the conference in Ref. 53.	